Local shear transformations in deformed and quiescent hard-sphere colloidal glasses

Local shear transformations in deformed and quiescent hard-sphere colloidal glasses

K. E. Jensen*

Department of Physics, Harvard University, Cambridge, MA, 02138

D. A. Weitz

Department of Physics, Harvard University, Cambridge, MA, 02138 and

School of Engineering and Applied Sciences,

Harvard University, Cambridge, MA, 02138

F. Spaepen†

School of Engineering and Applied Sciences,

Harvard University, Cambridge, MA, 02138

(Dated: July 31, 2014)

Abstract

We performed a series of deformation experiments on a monodisperse, hard-sphere colloidal glass while simultaneously following the 3D trajectories of roughly 50,000 individual particles with a confocal microscope. In each experiment, we deformed the glass in pure shear at a constant strain rate ($1 - 5 \times 10^{-5}$ s^{-1}) to maximum macroscopic strains ($5 - 10\%$), then reversed the deformation at the same rate to return to zero macroscopic strain. We also measured 3D particle trajectories in an identically-prepared quiescent glass in which the macroscopic strain was always zero. We find that shear transformation zones exist and are active in both sheared and quiescent colloidal glasses, revealed by a distinctive four-fold signature in spatial autocorrelations of the local shear strain. With increasing shear, the population of local shear transformations develops more quickly than in a quiescent glass, and many of these transformations are irreversible. When the macroscopic strain is reversed, we observe partial elastic recovery, followed by plastic deformation of the opposite sign, required to compensate for the irreversibly transformed regions. The average diameter of the shear transformation zones at maximum strain is 2.3 particle diameters.

* kjensen@post.harvard.edu

† spaepen@seas.harvard.edu

I. INTRODUCTION

When an external stress is applied to a material, it deforms: first elastically (reversibly), then plastically (irreversibly) when strained beyond the yield point. While the mechanisms of deformation in crystalline materials have been well understood for decades, a similar understanding of the deformation mechanisms in amorphous materials remains a topic of intense research. Theory [1–4] and simulation [5–9] predict the existence of "flow defects" or "shear transformation zones" that govern plastic deformation in glasses as dislocations do in crystals. However, unlike dislocations, which are readily observable as defects in an otherwise-regular crystal structure, the corresponding entities in glasses are difficult to observe directly in the amorphous structure, and a full understanding of their nature and origin is lacking. This insight is particularly important for understanding the deformation and failure mechanisms of bulk metallic glasses, a relatively new class of strong materials that show considerable promise for structural applications [10].

An ideal experiment to investigate deformation mechanisms in a glass would simultaneously follow the microscopic and macroscopic dynamics during deformation. In atomic and molecular glasses, however, the constituent elements are simply too small and move too quickly for this ideal experiment to be possible. Colloidal glasses provide unique experimental systems for probing the structure and dynamics of glasses over the complete range of length scales from the individual colloidal particles up to the bulk amorphous material [11, 12]. Monodisperse, hard-sphere colloidal particles can easily be made to form glasses by sedimentation onto flat or patterned substrates, with the resulting structure dependent on the deposition flux and the boundary condition imposed by the substrate [13]. The relative ease of both structure formation and detailed observation in 3D using optical microscopy makes colloidal glasses ideal for studying structure-property relations in a generic amorphous solid. Experiments on the deformation of hard-sphere colloidal crystals proved to be in excellent agreement with classical dislocation theory [14–18], which gives us confidence that these systems provide a reliable scaled-up picture of phenomena on the atomic level.

Experiments on hard-sphere colloidal glasses under shear deformation [11, 19] identified shear defects as localized regions of high irreversible strain, and concluded that they can be described by Eshelby's analysis [20, 21] of a highly strained inclusion coupled to an elastic, isotropic surrounding medium. For a shear transformation of a spherical inclusion of radius

a with unconstrained transformation shear strain $\epsilon_{yz}^T = \gamma/2$ and the same elastic properties as its surroundings, the shear strain field in the y-z plane is

$$\epsilon_{yz}(\mathbf{r}) = \begin{cases} \epsilon_{yz}^0, & r < a \\ \frac{\epsilon_{yz}^0 a^3}{4r^5}\left(9a^2c - (2+3c)r^2 - 15c(7a^2 - 5r^2)\cos(4\theta)\right), & r \geq a \end{cases} \tag{1}$$

where $c = 1/(4(4-\nu))$ is a dimensionless elastic constant, with ν Poisson's ratio, $\mathbf{r}(y,z)$ the position vector with origin at the center of the inclusion, and $\theta = \cos^{-1}(z/r)$. Details of the derivation and the full three-dimensional expression are given in the Appendix (Equation A.5).

The $\cos(4\theta)$ dependence of the strain field outside the inclusion produces a characteristic four-fold pattern in the y-z plane. The presence of this pattern is the signature that Eshelby inclusions are active in the material. Experimentally, the strain field is analyzed by its autocorrelation function. Figure 1 shows the 3D spatial autocorrelation function of the analytic ϵ_{yz} strain field of Equation A.5 on the three orthogonal coordinate planes. The plot on the y-z plane maintains the characteristic four-fold symmetry. Recent experiments observed this four-fold signature in spatial autocorrelations of local strain measured for a density-matched PMMA colloidal glass during steady-state homogenous deformation [19]. The same signature was also recently seen in 2D simulations of supercooled liquids under shear [9].

However, much remains unknown about these shear transformation zones that behave as Eshelby inclusions: Do they exist in the absence of applied strain? How does their population evolve with time and applied strain? What happens to these defects when the macroscopic applied strain is reversed?

Here, we show that shear transformation zones are active in both sheared and quiescent (i.e. undeformed) colloidal glasses. We confirm that these regions are Eshelby-type inclusions. In the absence of applied strain, shear transformation zones are thermally activated in all directions and produce zero macroscopic strain. When a uniform macroscopic shear strain is applied to the glass beyond the yield point, a fraction of these shear defects transforms irreversibly in the direction of the applied shear. When the applied macroscopic strain is reversed, we observe an initial elastic recovery followed by plastic deformation governed by inclusions of the opposite sign until the macroscopic strain has fully returned to zero.

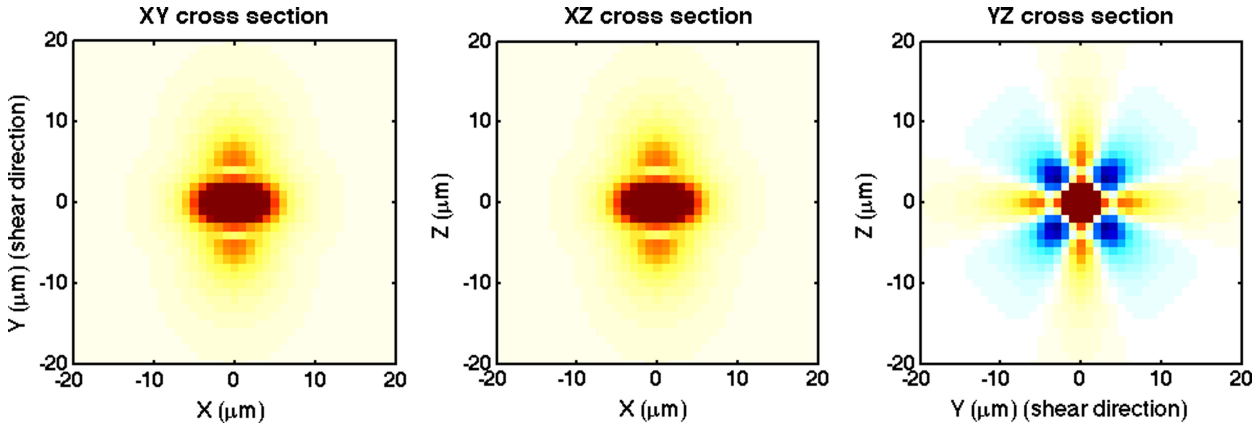

FIG. 1. (Color online) (a) x-y, (b) x-z, and (c) y-z cross-sections of the 3D spatial autocorrelation function of the ϵ_{yz} analytic strain field for a single, ideal Eshelby inclusion of radius 2.25 μm embedded in an infinite isotropic elastic medium with Poisson ratio $\nu = 1/3$. This three-dimensional correlation pattern with its characteristic four-fold pattern in the y-z plane is the signature of Eshelby inclusions active in an elastic matrix.

II. EXPERIMENTS

We perform experiments with hard-sphere colloidal silica particles with a polydispersity <3.5% and diameter $2R = 1.55$ μm [22] in a mixture of dimethyl sulfoxide (DMSO, 62.8% by volume), deionized water (36.0% by volume), and fluorescein-NaOH dye solution (1.2% by volume). The particles have nearly twice the density of the surrounding fluid, with a density difference of $\Delta\rho = 0.94$ g/cm^3. The Peclet number for sedimentation at room temperature under Earth's gravity is $Pe = \Delta\rho g R^4/(k_B T) = 0.83$, which means that the rates of sedimentation and diffusion are similar. The dye solution is 3% by weight fluorescein-NaOH in water, which both enables fluorescent imaging of the sample and reduces the Debye screening length of the particles to less than 10 nm. The fluid phase matches the index of refraction of the particles and has a viscosity $\eta = 1.6$ mPa·s.

We prepare colloidal glasses directly in the sample cell by high-flux sedimentation at $1g$ onto the amorphous template, starting from an initial volume fraction, ϕ_0, of about 3.5%. These conditions result in a dimensionless deposition flux of $\phi_0 Pe = 0.03$, which corresponds to a very slow quench rate, just high enough to ensure glass formation [13], so that we form as relaxed and low-energy a glass as possible. After sedimentation is complete, the colloidal glass has a total thickness of about 250 μm. The volume fraction at the bottom of the

sediment, where the experiment takes place, is $\phi = 62\%$ as measured by particle counting. A radial distribution function, $g(R)$, of one of the systems studied is shown in Figure 2. We verify that there are no crystalline regions present anywhere in the sample by directly imaging the entire shear gap throughout the experiment.

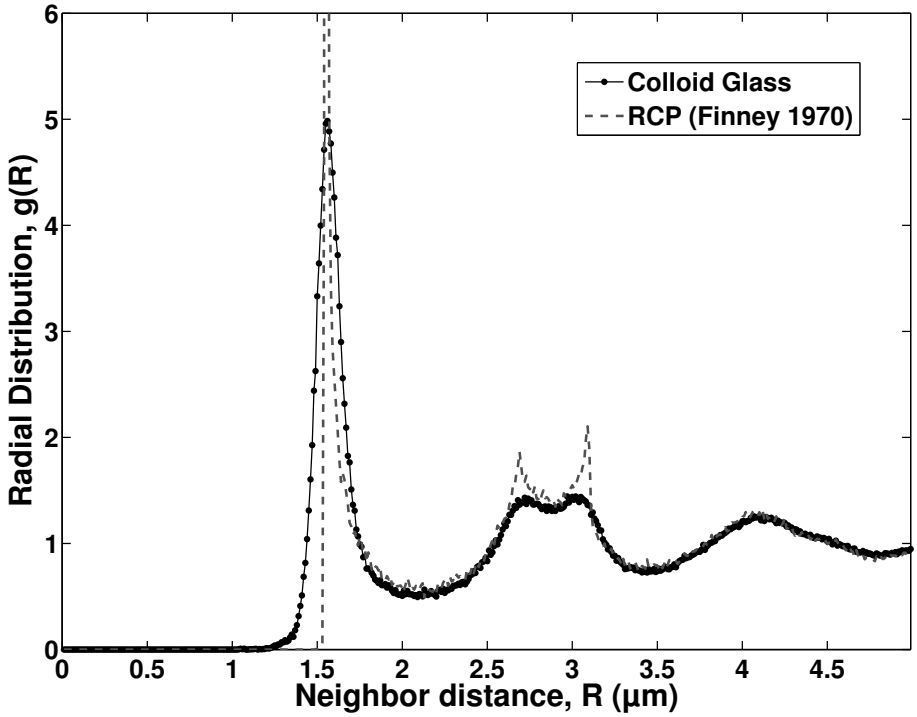

FIG. 2. Radial distribution function, $g(R)$, of the colloidal glass (dots). The radial distribution of Finney's random close packing [23] (dashed line), scaled for the same particle diameter, is shown for comparison.

We apply deformation to colloidal glasses with a shear apparatus that allows simultaneous three-dimensional imaging of the individual colloidal particles with a confocal microscope. A schematic of the shear apparatus is shown in Figure 3. The colloid is contained in a cylindrical metal sample reservoir $\sim$1 cm in diameter that is integrated into the shear apparatus. The reservoir is sealed at the bottom by a 0.17-mm-thick glass coverslip affixed with glue. This coverslip is lithographically patterned with an amorphous template etched into the glass that prevents crystallization of the sample during glass formation [24]. The entire shear cell apparatus, including the sample reservoir, is fixed to the microscope stage and does not move over the course of the experiment.

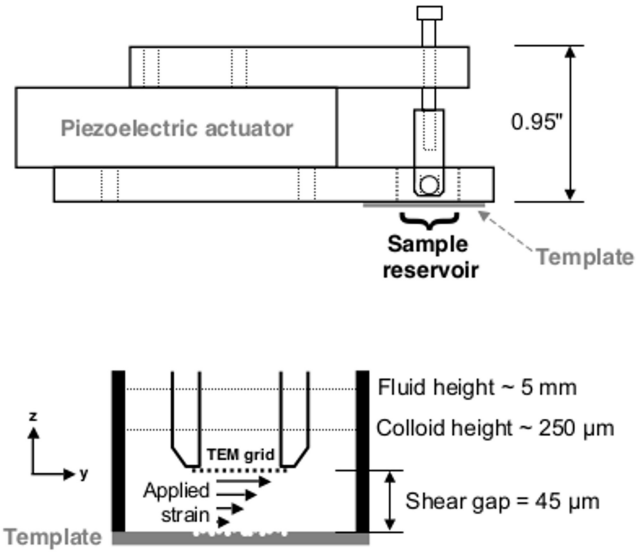

FIG. 3. Top: Side view of the assembled shear cell, drawn to scale. Shear is applied to a sample in the reservoir with a piezoelectric actuator that is mechanically coupled to the sample via a height-adjustable post. Bottom: Cross section schematic of the sample reservoir, not to scale. Shear can be applied positively or negatively along the y-direction.

We use a computer-controlled piezoelectric actuator to apply the shear deformation. The actuator has a maximum travel of 80 μm in the y-direction, and an accuracy ± 5 nm. It is mechanically coupled to the glass by a perforated, hollowed-out metal cylindrical post with a fine gold, 300-mesh transmission electron microscope (TEM) grid that spans the bottom of the post. The TEM grids have a bar width of 10 μm and a 73 μm empty spacing between the bars, so that the grid does not interfere with the sedimentation process. The height of the grid is adjustable by a #2-56 screw that moves the post vertically. The shear gap, Δz, is the separation between the bottom of the TEM grid and the amorphous template. In the experiments reported here, the gap was $\Delta z = 45$ μm. The maximum available strain rate is about 10^{-2} s^{-1}, limited by the step sizes for the piezo having to be small compared to the particle size and by the maximum communication rate from the computer to the piezo controller. However, because we are interested in homogenous deformation, all of our experiments are conducted well below this upper limit.

The entire shearing setup is assembled and the shear gap geometry fixed prior to the introduction of the initially-dilute colloid. Sedimentation is complete within about two hours, after which the glass is allowed to relax further for six hours. By quenching the glass

directly in the sample cell, we ensure that the glass has never experienced any strain prior to the experiment. This procedure embeds the TEM grid deep inside the sample, about 200 μm below the surface of the sediment, ensuring strong contact between the colloid glass and the TEM grid as the glass completely surrounds the bars of the grid and fills the space above and below it.

Each deformation experiment consists of a single strain cycle: we apply a uniform macroscopic y-z shear strain to the glass at a strain rate $\dot{\gamma}$, up to a maximum macroscopic strain γ_{max}, then reverse the deformation at an equal, but opposite, strain rate until the macroscopic strain returns to zero. A period of quiescence follows each deformation experiment before the start of the next one. We will focus most of our discussion on a single, representative experiment taken from a sequence of five consecutive independent plastic deformation experiments: Experiment 1, to $\gamma_{max} = 5.0\%$ at $\dot{\gamma} = 5.0 \times 10^{-5}$ s^{-1}; Experiment 2, to $\gamma_{max} = 10.0\%$ at $\dot{\gamma} = 5.0 \times 10^{-5}$ s^{-1}; Experiment 3, to $\gamma_{max} = 10.0\%$ at $\dot{\gamma} = 2.0 \times 10^{-5}$ s^{-1}; Experiment 4, to $\gamma_{max} = 5.0\%$ at $\dot{\gamma} = 5.0 \times 10^{-5}$ s^{-1} (a repeat of Experiment 1); and Experiment 5, to $\gamma_{max} = 5.0\%$ at $\dot{\gamma} = 2.0 \times 10^{-5}$ s^{-1}. Between each experiment, the glass sample was quiescent for 1000 seconds, during which time we continued to image the particles. All of these strain rates are slow enough to ensure homogeneous deformation, as confirmed by the strain measurements and direct observation. The maximum macroscopic strains exceed the measured yield point of this colloid glass, $\gamma_{yield} \approx 2\%$ [25, 26], as well as that of metallic glasses, which are the closest atomic analog [27].

Here, we focus on the results of the slowest 10% maximum strain experiment, Experiment 3, because this gives us the best time resolution. We additionally include results from the other 10% strain experiment, Experiment 2, for the purpose of comparing the effects of strain rate. Finally, we report observations on a quiescent glass to which we never applied strain, but which had otherwise identical preparation and experimental conditions as the deformed glass.

Although the strain we apply is cyclic, it is important to note that these are not oscillatory strain experiments. Oscillatory strain experiments [28–30] and simulations [31–33] typically involve deforming a glass through large numbers of strain cycles toward a steady-state oscillation, also usually at strain rates that are orders of magnitude higher than in our experiments. Our experiments focus on the initial deformation of a glass at very low strain rates, and we reverse the strain in order to probe the reversibility of the local deformations.

All samples are imaged from below in three dimensions using a Leica SP5 point-scanning confocal microscope. All image stacks are taken far from the edges of the template and from the sample cell walls to avoid possible boundary effects. During deformation experiments, we take two image stacks at each time step: a low-resolution stack that spans the entire shear gap, and a high-resolution image stack in the middle of the shear gap, about 10 μm away from either top or bottom of the gap. The low-resolution images allow us to monitor the entire shear gap and verify that there is no slip at either the amorphous template or the TEM grid, nor are there any inhomogeneous shear effects that might change the effective applied strain. The high-resolution stack provides the data that we use for locating the particles and subsequent analyses. Figure 4 shows an example composite y-z cross section through the raw image data, with the high-resolution central region overlaid on the low-resolution stack. It takes about 5.5 minutes to acquire both stacks and we repeat the scans every 6 minutes. This is fast enough at the applied strain rates for each image stack to represent a snapshot of the particle configuration at that time.

III. RESULTS

From the raw stacks of confocal images, we locate the centers of all particles in three dimensions using standard particle location software [34], run iteratively to minimize missed or doubly-located particles [24]. We then convert the coordinates from units of pixels to micrometers using an experimentally calibrated conversion factor [35]. Finally, we link the particle locations over time into 3D trajectories, including trajectories that begin or end as particles near the edge move in or out of the field of view. These trajectories are the basis of all subsequent analyses.

The vector displacements of each particle's nearest neighbors between a reference time, t_{ref}, at the beginning of the experiment and some later time, t, sample the displacement field in the vicinity of each particle since t_{ref}. Nearest neighbors are defined as all particles closer to a given particle than a distance equal to the first minimum of the radial distribution function (shown in Figure 2), and only neighbors that have moved no farther than the second neighbor shell at t are considered in strain calculations. From the neighbor displacements, we calculate [5] the local affine deformation tensor, α_{ij}, at each particle. By separating this tensor into its symmetric and antisymmetric parts, we obtain respectively the local strain, ϵ_{ij},

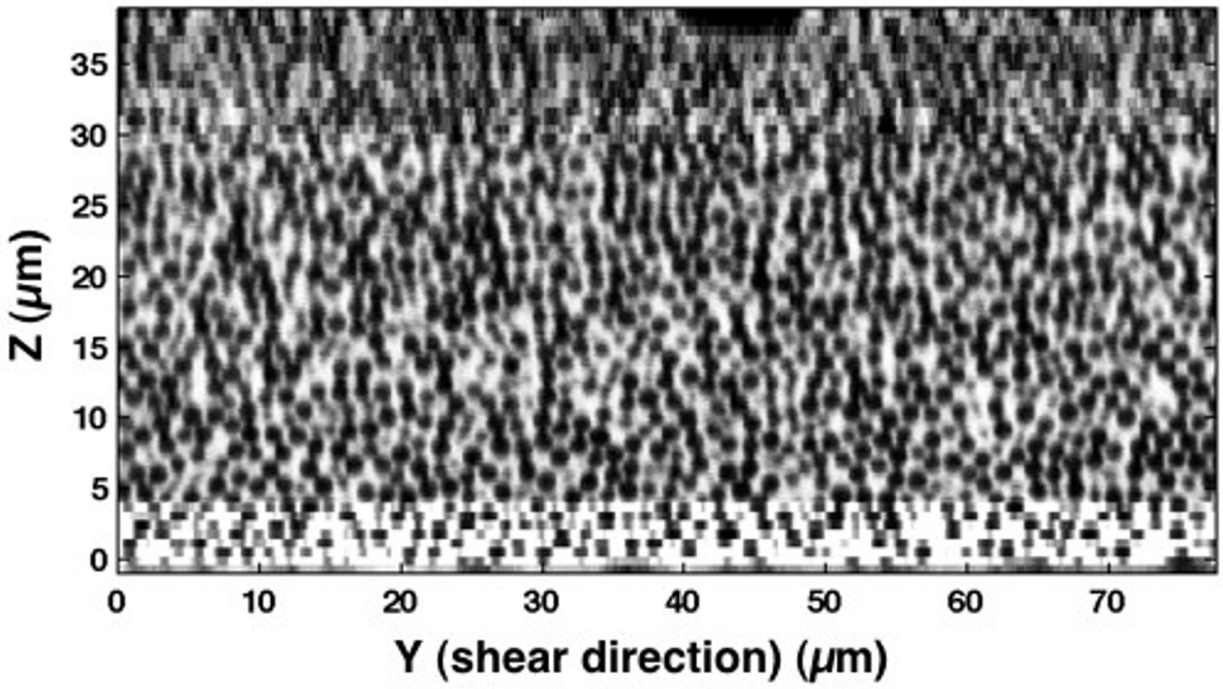

FIG. 4. Example of the confocal raw data, showing the high-resolution central stack (4.5 μm $\leq z \leq$ 30 μm) overlaid on the low-resolution stack that spans the entire shear gap from the stationary template to the moving TEM grid. Part of one of the bars of the TEM grid is visible in cross-section at the top of the image (40 μm $\leq y \leq$ 48 μm). The top of the amorphous template is just visible as dark bumps at the bottom of the image. A video of this cross section in motion during a deformation experiment is available online in the Supplemental Materials.

and rotation, ω_{ij}, tensors measured at each individual particle. A reconstruction of a small region of the glass with each particle colored according to its local ϵ_{yz} strain accumulated since the start of the experiment is shown in Figure 5a, with particles experiencing the largest strains drawn opaque.

During a deformation experiment, the externally-applied macroscopic strain is equal to the displacement of the piezoelectric actuator over time divided by the shear gap. We measure in two ways the macroscopic shear strain , γ, experienced by the sample since the reference time at the beginning of the experiment. First, from the slope of the deformation profile, which is a plot of the displacements of the individual particles as a function of height in the sample, as in Figure 5b. When the deformation profile is a straight line, as it is in our experiments, the macroscopic strain is uniform throughout the sample and equal to the

inverse of the slope of the line. Second, the macroscopic strain experienced by the sample is equal to twice the average local shear strain, $2\langle\epsilon_{ij}\rangle$. We find close agreement between the applied strain, the macroscopic strain obtained from the deformation profiles, and the average local y-z strain over time, as shown in Figure 5c. Figure 5c also shows that the other average shear strain components, $2\langle\epsilon_{xy}\rangle$ and $2\langle\epsilon_{xz}\rangle$, remain close to zero throughout the experiments. In quiescent experiments, all components of the average local strain remain near zero over time.

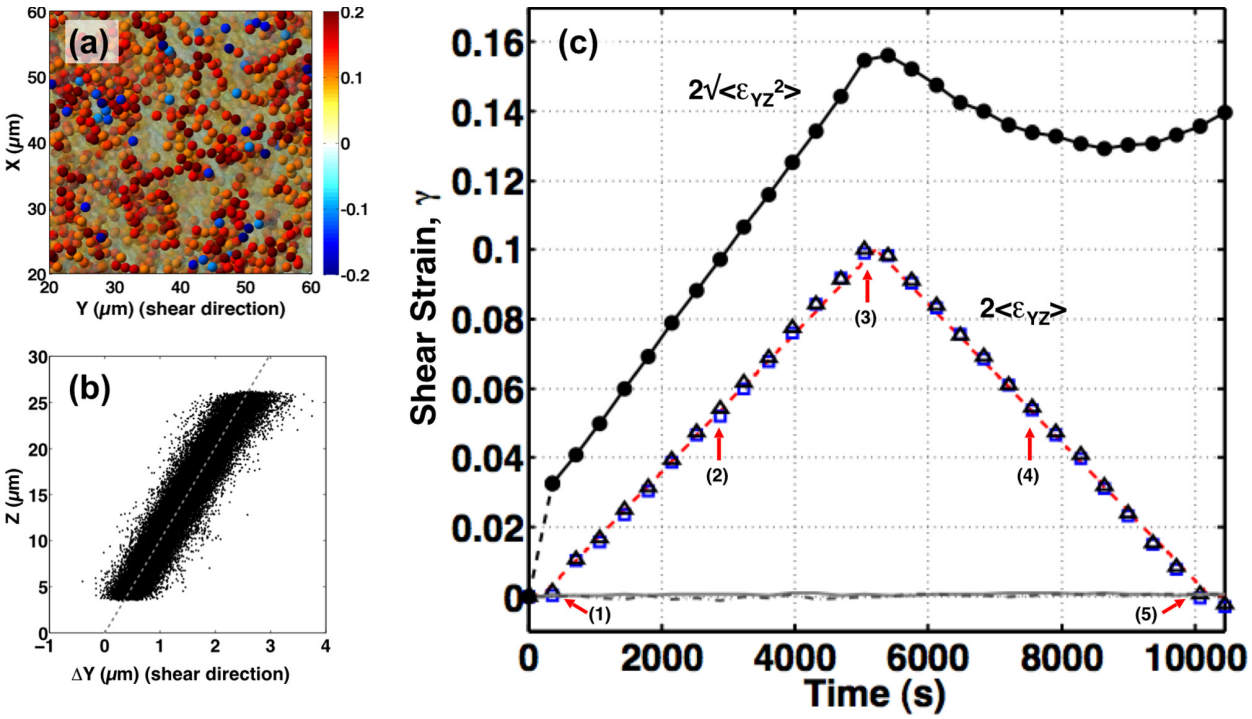

FIG. 5. (Color online) (a) Reconstruction of a small region of the colloidal glass when the applied strain was at its maximum, $\gamma_{yz} = 0.1$, marked as point (3) in (c). Particles in the reconstruction are colored according to their individual strain, ϵ_{yz}; those with $|\epsilon_{yz}| \geq 0.1$ are rendered opaque. (b) The deformation profile, z vs. Δy, at the same time, with a straight-line fit through the data. (c) The macroscopic strain measured in three ways: (red dashed line) the applied strain; (blue squares) by fitting the deformation profiles like (b); and (black triangles) the average of all the individual particle strains, $2\langle\epsilon_{yz}\rangle$. The measured strains orthogonal to the applied strain, $2\langle\epsilon_{xy}\rangle$ and $2\langle\epsilon_{xz}\rangle$, are shown as gray solid and dot-dashed lines, respectively. The RMS strain, $2\sqrt{\langle\epsilon_{yz}^2\rangle}$, is plotted as solid black dots.

The evolution of the macroscopic and local strain during deformation are shown in Figure

6, with the reference state for the strain set the beginning of the experiment prior to any applied strain. Each row in Figure 6 shows the results of measurements made at the times (1-5) indicated in Figure 5(c). Row (a) shows the measured deformation profiles. Row (b) shows top-view reconstructions of only those particles with the highest magnitude strain, colored according to the local ϵ_{yz} shear strain. Note that the strains at individual particles can significantly exceed the macroscopic strain, and that some even oppose the direction of the applied strain.

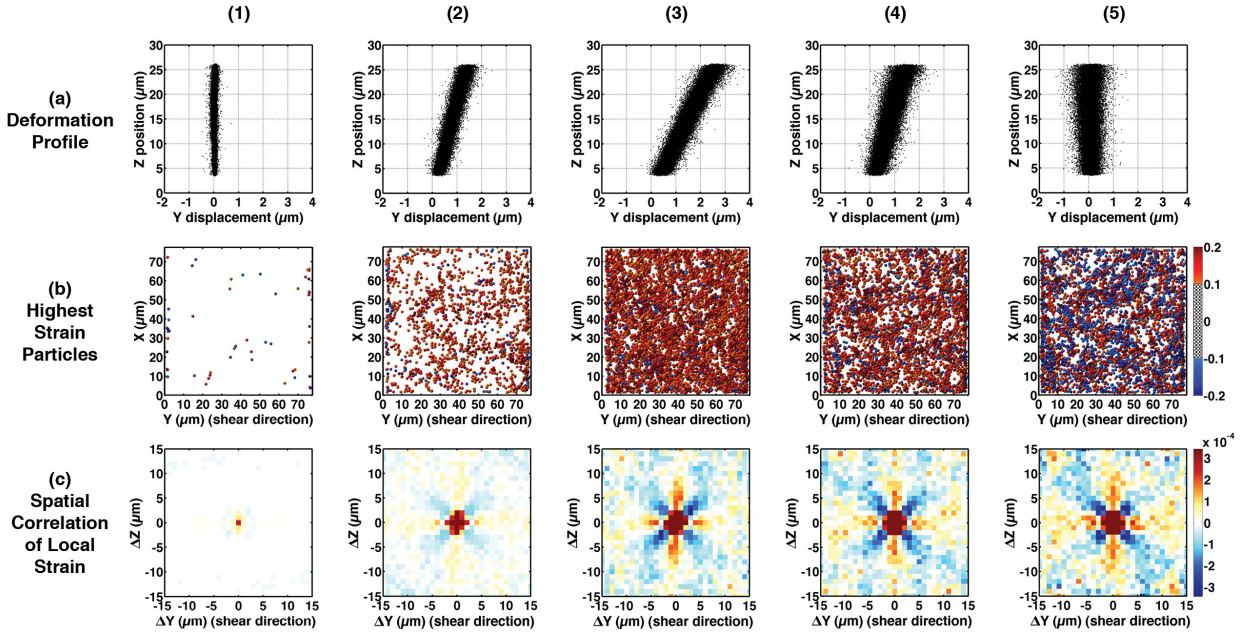

FIG. 6. (Color online) Evolution of strain and strain correlations in the colloidal glass during a shear experiment. The time and macroscopic strain corresponding to columns (1)-(5) are indicated in Figure 5c. Row (a): The deformation profiles. Row (b): Top-view reconstructions showing only those particles with individual strain $|\epsilon_{yz}| > 0.1$, colored according to their strain. On strain reversal, some of the regions of particles that acquire a high positive strain (red color) return to a low-strain configuration and disappear from the reconstruction; others experience an irreversible local deformation and remain in a high-strain state at the end of the experiment. These are compensated for by other regions that deform in the opposite direction (blue color), so that at the end the average strain is zero at time (5). Row (c): y-z plane cross-sections of ϵ_{yz} spatial autocorrelations, showing the evolution of the four-fold pattern that is the signature of Eshelby inclusions active in the material.

A similar summary of the evolution of the macroscopic and local strain during a quiescent experiment is shown in Figure 7. This figure shows measurements of the quiescent glass at the same time intervals as in Figure 6, although these times obviously have no particular significance in the quiescent experiment. In this experiment, the deformation profile broadens slowly, but remains vertical and centered at zero over time. We observe a coarsening and heterogeneity of the local strain field over time that is similar to that observed in the deformation experiment, but which develops more slowly.

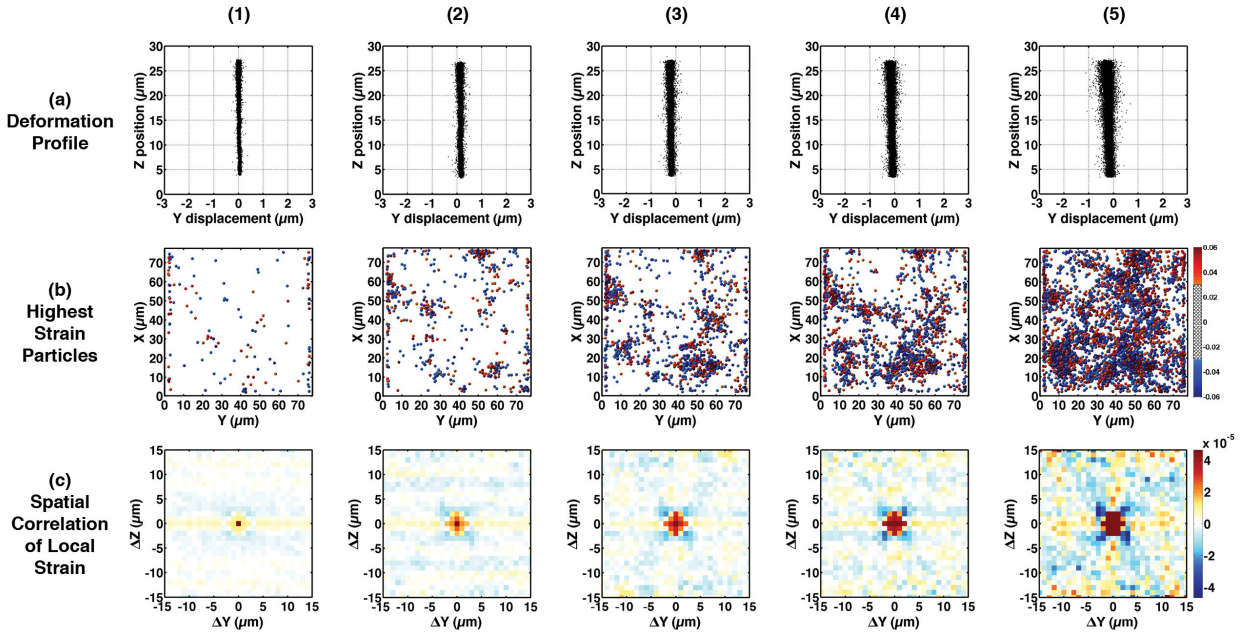

FIG. 7. (Color online) Evolution of strain and strain correlations in a quiescent colloidal glass. The time intervals are chosen to match those of Figure 6, although these times have no particular significance in the quiescent experiment. Row (a): The deformation profiles, showing broadening but no deformation. Row (b): Top-view reconstructions showing only those particles with individual strain $|\epsilon_{yz}| > 0.03$, colored according to their strain. At any time, there are equal numbers of high positive (red) and negative (blue) particles. Row (c): y-z plane cross-sections of ϵ_{yz} spatial strain correlations, showing the evolution of the four-fold Eshelby signature. The position axes for all figures are identical to the corresponding plots in Figure 6. Rows (b) and (c) have smaller color scales in this figure.

We quantify this evolving heterogeneity of the local strain field by computing the root-mean-square (RMS) strain over time, averaged over all the particles, $2\sqrt{\langle \epsilon_{yz}^2 \rangle}$. During the

quiescent experiment, the RMS strain increases linearly with time with a slope of 0.59×10^{-5} s^{-1}. This reflects a steady coarsening of the local strain field, corresponding to a steady broadening of the distribution of local strains about a mean macroscopic strain of zero (Figure 7(a)).

With applied shear deformation, the RMS strain evolves differently. During the initial macroscopic deformation from zero to γ_{max}, the measured RMS strain experienced by the glass increases linearly at 2.6×10^{-5} s^{-1}, significantly faster than the background thermal rate. The RMS of $\epsilon_\delta(\mathbf{r}) = \epsilon(\mathbf{r}) - \langle\epsilon(\mathbf{r})\rangle$, the local strain minus the macroscopic strain, this also increases linearly with time, at a rate of 1.8×10^{-5} s^{-1}, three times faster than in the quiescent sample. On strain reversal, however, the RMS strain actually decreases to a minimum over several percent recovered strain, then begins to rise again before the macroscopic strain returns to zero. The amount of RMS strain recovery and the macroscopic deformation over which the recovery occurs is independent of strain rate at the relatively slow strain rates used in our experiments, as shown in Figure 8.

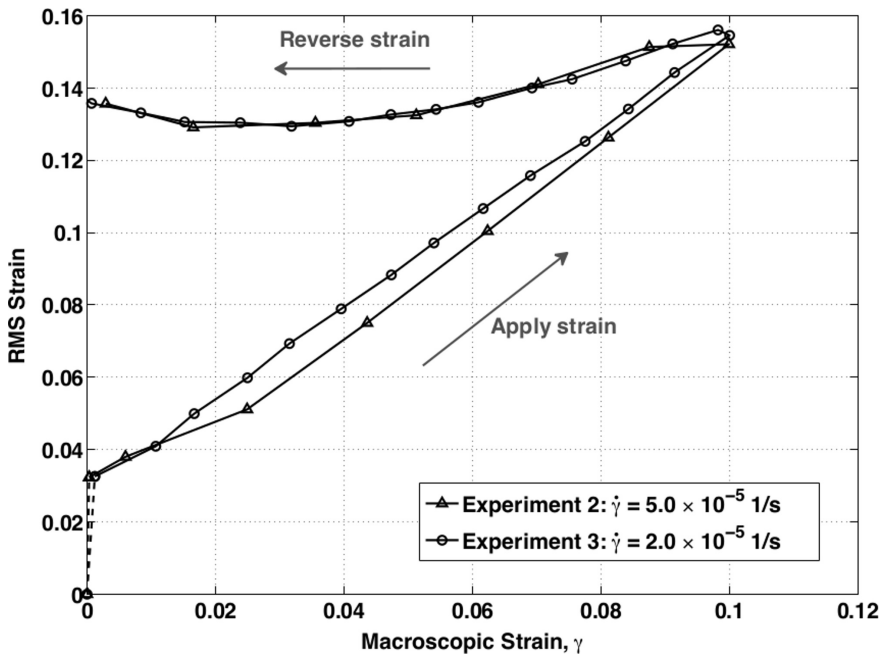

FIG. 8. RMS strain vs. macroscopic strain for Experiments 2 and 3. These had the same maximum strain ($\gamma_{max} = 10.0\%$) but strain rates that differed by a factor of 2.5.

We look for patterns in the evolution of local particle strain by computing the unnormalized three-dimensional spatial autocorrelation [9, 19] of the zero-mean local strain field

per particle, $C_\epsilon(\mathbf{\Delta r}) = \langle \epsilon_\delta(\mathbf{r})\epsilon_\delta(\mathbf{r}+\mathbf{\Delta r})\rangle$, where $\mathbf{\Delta r}$ are all of the interparticle distances. The results are shown in y-z cross-section in Figure 6c as they evolve over the course of the experiment. The three orthogonal cross-sections at maximum strain are shown in Figure 9. For consistency, we use a fixed color scale of $\pm 0.1\langle\epsilon_\delta\rangle_{max}$ for all of these plots, chosen so that the pattern with the maximum dynamic range would be shown clearly.

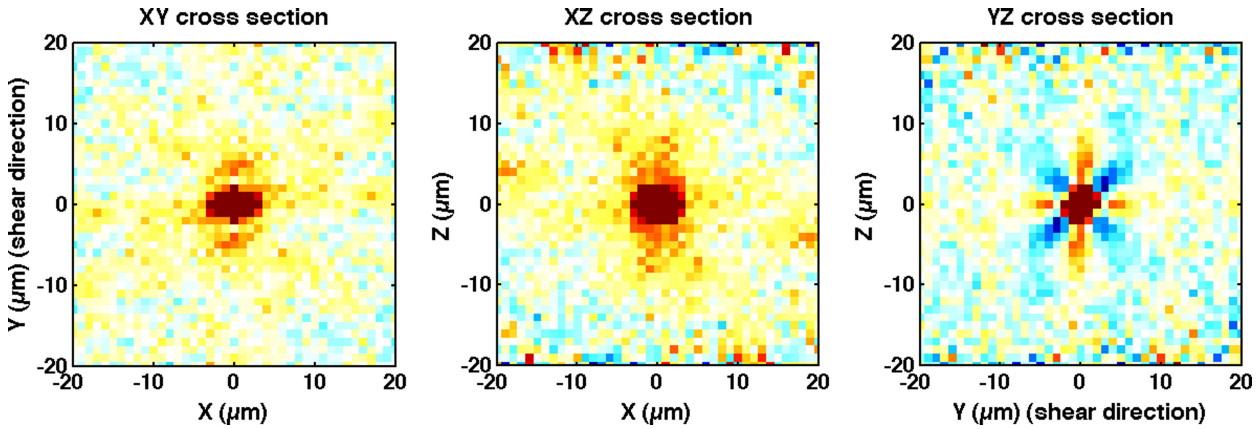

FIG. 9. (Color online) (a) x-y, (b) x-z, and (c) y-z plots of the spatial autocorrelations of the ϵ_{yz} strain field at maximum applied strain ($\gamma_{max} = 10.0\%$, $t = 5040$ seconds), revealing the characteristic 3D structure of an Eshelby inclusion (shown in Figure 1).

A distinct four-fold pattern is apparent in the strain correlations. With a more sensitive color scale, the four-fold pattern is visible even in the first measurement, at which time no macroscopic strain has yet been applied. Over time, the four-fold pattern becomes quite pronounced. In Figure 6, we see that the four-fold pattern remains strong even after the macroscopic strain is completely reversed.

We quantify the development of the Eshelby core and surrounding pattern in the y-z strain field correlations by taking azimuthal averages in the y-z plane of the 3D spatial strain autocorrelation. These results are shown in the upper plot of Figure 10 for the same five time points as in the previous figures. The curves in the upper plot of Figure 10 show that the average inclusion core size increases somewhat with time during the initial, positive deformation, and does not reduce in size on strain reversal. By comparing the zero-crossing and the position of the minimum of the azimuthal average to the analytic calculation, we estimate the average inclusion core radius to be 1.8 μm, consistent with earlier observations [11]. An example of a specific inclusion with a slightly larger core radius is shown in Figure 11.

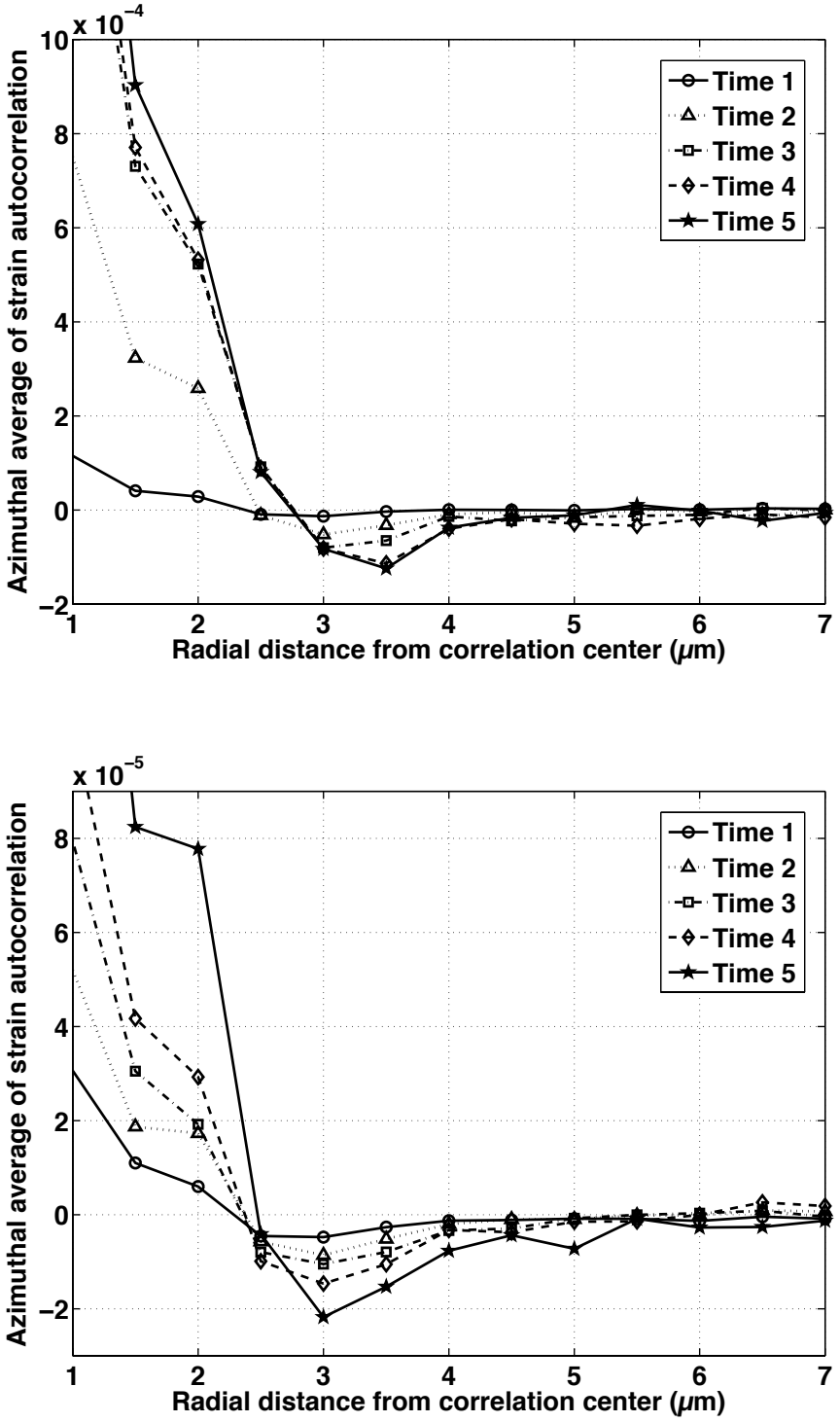

FIG. 10. Azimuthal average of the y-z spatial strain field autocorrelation in the y-z plane versus radial distance from the correlation center for both the sheared and quiescent samples (top and bottom, respectively). The times refer to Figure 5(c). Note that the vertical axis for the sheared plot is 10x that of the quiescent plot; this is due to the slower evolution of local strain in the quiescent sample.

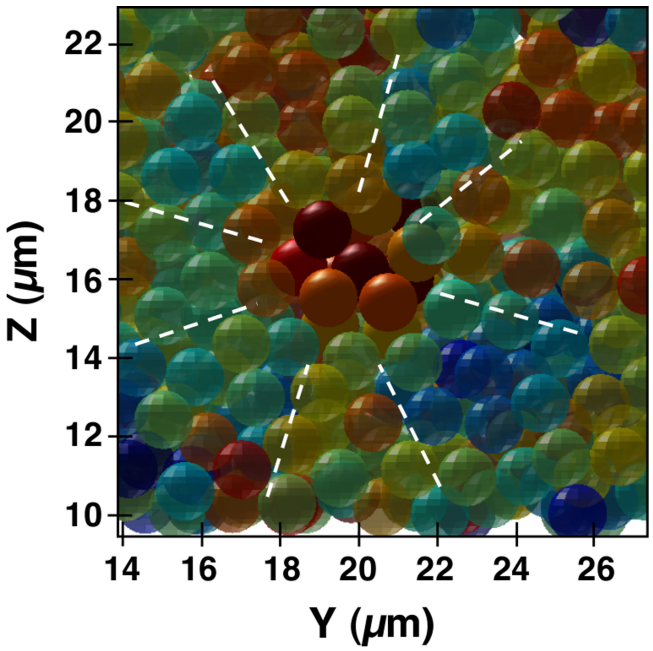

FIG. 11. (Color online) Example of an Eshelby inclusion (opaque) and its surroundings (semi-transparent) reconstructed from an experiment with a hard-sphere glass deformed at slightly under $\dot{\gamma} = 10^{-5}$ s^{-1}. Particles are colored according to their local shear strain, ϵ_{yz}, with red indicating high positive strain and blue indicating negative strain. Dashed lines approximately indicate the four-fold alternating positive and negative strain field surrounding the inclusion.

Remarkably, the same four-fold signature appears in the spatial correlations of the local shear strain in the quiescent sample, even though there is no applied strain. These correlations are shown in y-z cross-section in Figure 7c as they evolve over time, and all three orthogonal cross-sections at the final time are shown in Figure 12. Again, we use a fixed color scale of $\pm 0.1 \langle \epsilon_\delta \rangle_{max}$ for these plots; note, however, that in the quiescent sample, $\langle \epsilon_\delta \rangle_{max}$ is almost ten times smaller than in the sheared sample, and so the color scale is accordingly different than in the figures for the sheared sample. We also show the azimuthal averages of the strain autocorrelation for the quiescent sample in the lower plot of Figure 10. We observe that the four-fold pattern appears more slowly than in the deformed sample, the magnitude of the correlations is smaller after the same time intervals, and the inclusion core is slightly smaller. To confirm that this signature is the result of correlated motions and cannot arise from random displacements, we computed the strain fields and spatial correlations for simulated Gaussian-distributed displacements from the positions of the reference

glass (standard deviations 1% to 20% of the particle diameter) and found no such signature.

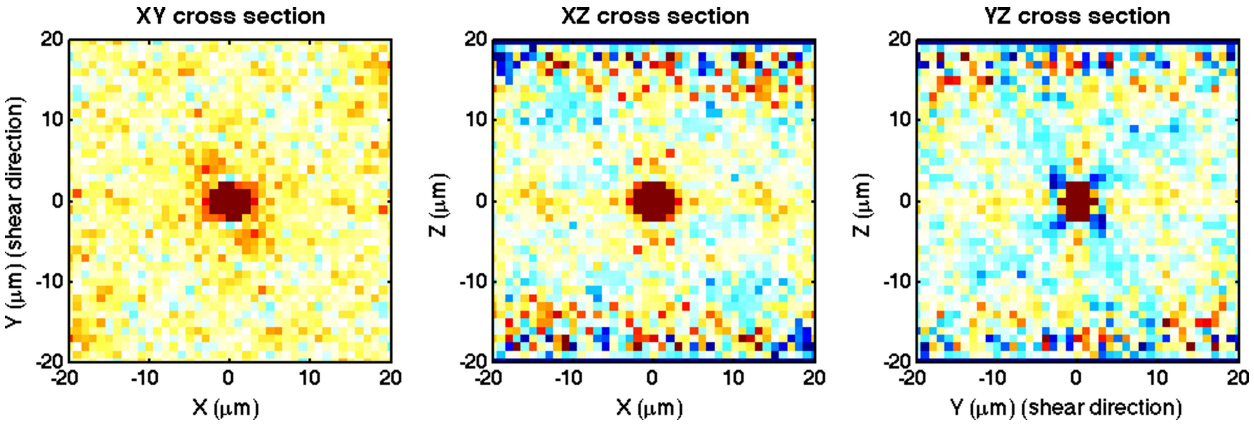

FIG. 12. (Color online) (a) x-y, (b) x-z, and (c) y-z plots of the spatial autocorrelations of the ϵ_{yz} strain field at the longest time interval (corresponding to Figure 7, column 5). The correlations in the quiescent glass exhibit the same characteristic 3D structure as those for the calculated strain of an Eshelby inclusion (Figure 1).

IV. DISCUSSION

The deformation profiles demonstrate that the macroscopic strain experienced by the glass is homogenous during the deformation experiments. Some regions, however, undergo significantly higher than average local strain. These are the "flow defects" or "shear transformation zones" that govern plastic deformation in the glass. We can see examples of these and their strain fields directly, as in the example of Figure 11 and in earlier work [11], but their presence is most apparent in the spatial correlations of the local strain field. The four-fold pattern of alternating positive and negative correlation surrounding the positive core in the plane of that shear strain component is the characteristic signature that these local high-strain regions transform as Eshelby inclusions. Over time, the four-fold Eshelby signature strengthens, corresponding to an increasing concentration in the material of regions that have transformed as Eshelby inclusions since the start of the experiment. That the Eshelby signature remains dominant in the correlations over time and with applied strain indicates that these inclusions are the dominant plastic deformation mechanism in the glass.

Interestingly, we observe the same four-fold Eshelby signature in quiescent glass strain field correlations. This means that the same sort of defects exist and are active in the qui-

escent glass, where only thermal energy is available to drive the transformations. However, the inclusion activation is slower than in the deformed glass and we observe significantly less motion over the same time intervals; the correlation signature, breadth of the displacement profile, and RMS strain all grow more slowly in the quiescent experiment than in its deformed counterpart. Further, without any applied strain to provide a directional bias, the purely thermally-activated inclusions in the quiescent sample produce no macroscopic strain.

Deformation of a material has elastic and plastic components. Upon reversal of the strain, if the deformation were purely elastic, we would expect all of the local strain to be fully reversible, and the particles to return to their initial positions. If the deformation were purely plastic, we would expect to see no reversibility; rather, the strain reversal would simply cause plastic deformation to begin immediately in the opposite direction. We observe an intermediate behavior: partial elastic recovery followed by new plastic deformation in the reverse direction. This behavior is characteristic of a material that has been loaded elastically and then driven beyond its yield strain [26] prior to strain reversal.

From the reconstructions of local strain in row (b) of Figure 6, we see directly that the local strain is reversed in two ways. Some regions that attained a high local strain (colored red) disappear from the reconstruction as the strain is reversed (times (3) to (4)). In these locations, the strain was locally *reversible*, and when the applied strain was reversed the particles returned very nearly to their original configurations. In other regions, the local strain was *irreversible*; these regions retain a high positive local strain (red) even when the macroscopic strain has returned to zero. To compensate, other regions transform with high-magnitude strain in the opposite sense (blue) so that the average strain remains equal to the applied strain. As the strain is reversed, the four-fold Eshelby signature remains strong because of the irreversibly transformed regions. As plastic deformation eventually begins in the opposite direction, the new, negative inclusions also contribute positively to the spatial strain correlation [9].

The decrease in RMS strain observed on strain reversal (times (3) to (4)) results from recovery of stored elastic displacements. Once all the stored elastic strain has been reversed, the glass is in a state of zero stress, but still has a net positive strain from the irreversible plastic deformation that it experienced after yield. In order to return to net zero macroscopic strain, the glass must undergo new plastic deformation in the reverse direction to

undo this residual strain. This causes the subsequent rise in the RMS strain late in the experiment as the macroscopic strain is driven to zero. The RMS strain does not return to zero precisely because the material has undergone irreversible internal rearrangements that are not undone by reversing the macroscopic strain. We do not expect a perfect return to zero RMS strain even below yield, because there always exists some thermal background of local shear transformations, as the quiescent experiment demonstrates. However, since the maximum strain in our deformation experiments is beyond yield, the RMS strain is driven well above the thermal background, and does not recover even to the thermal background on strain reversal.

In the core of the inclusions, where the strains are largest, the deformation is less affine than in the surrounding matrix, where the strains are smaller. Because the strains in the matrix are more affine, it is still possible to obtain a clear four-fold autocorrelation pattern, even with a considerable non-affine deformation in the core.

V. CONCLUSION

We followed the 3D trajectories of roughly 50,000 individual particles in colloidal glasses under conditions of quiescence and applied shear deformation. We measured the macroscopic and local strain in the glasses, and observed an evolving four-fold pattern in spatial autocorrelations of the local strain field, both with and without deformation. These four-fold patterns indicate that the dominant deformation mechanisms in the glass are shear transformation zones that behave as Eshelby inclusions: local regions of high plastic strain that couple elastically to the surrounding material. These inclusions exist and are active even in the absence of applied strain; the available thermal energy can be sufficient to activate them, although without any directional bias they contribute no macroscopic strain.

With applied strain, we find that the Eshelby signature evolves more quickly. The applied shear stress biases the population of inclusions in the direction of the applied strain, so that they contribute to the macroscopic deformation. When the glass is strained beyond yield, many of the local transformations are irreversible and result in permanent plastic deformation. These contribute a net positive strain from within the material. The result is a permanent four-fold Eshelby signature in the strain correlations and an RMS strain that remains above the thermal background even when the macroscopic strain has returned to

zero. As we drive the material back to zero macroscopic strain, these irreversibly transformed regions are compensated by the activation of inclusions with a negative internal strain. The average diameter of the inclusions at 10% shear strain is 2.3 particle diameters.

The RMS strain also increases faster with applied strain than it would just from the available thermal energy; on strain reversal, the RMS strain drops to a local minimum over several percent strain recovery until the glass attains a state of zero stress. The drop in RMS strain corresponds to a decrease in the energy stored in the strain field; the elastic energy that was stored in the glass during its initial, elastic loading is being recovered. Finally, the RMS strain starts to rise again as the glass begins to deform plastically in the opposite direction. Because this is the only way that net zero macroscopic strain can be reached, it causes a new increase in the RMS strain since the negative-strain inclusions contribute positively to the RMS strain.

The regions that can transform as Eshelby inclusions exist and can be thermally activated in a quiescent glass. We have also directly observed additional examples in our experiments of particle clusters that directly exhibit the strain signature of the Eshelby four-fold pattern, such as the one shown in Figure 11.

Appendix: Analytic Strain Fields

Eshelby calculates the three-dimensional displacements for a spherical inclusion with an unconstrained transformation shear strain $\epsilon_{yz}^T = \gamma/2$ and inclusion radius a in an isotropic elastic medium with dimensionless elastic constant $c = 1/(4(4-\nu))$. Here, ν is Poisson's ratio, taken to be 1/3 for this colloidal glass [11, 13].

The shear strain inside the inclusion when it is embedded in the elastic matrix is

$$\epsilon_{yz}^0 = \gamma \frac{4-5\nu}{15(1-\nu)} \tag{A.1}$$

For such an inclusion, the displacements at distances $r = \sqrt{x^2+y^2+z^2}$ outside the inclusion are

$$u_x = \epsilon_{yz}^0 a^3 \left\{ 6c(r^2-a^2)\left(\frac{5xyz}{r^7}\right)\right\} \tag{A.2}$$

$$u_y = \epsilon_{yz}^0 a^3 \left\{ \frac{z}{r^3} + 6c(r^2-a^2)\left(\frac{5y^2z}{r^7} - \frac{z}{r^5}\right)\right\} \tag{A.3}$$

$$u_z = \epsilon_{yz}^0 a^3 \left\{ \frac{y}{r^3} + 6c(r^2-a^2)\left(\frac{5yz^2}{r^7} - \frac{y}{r^5}\right)\right\} \tag{A.4}$$

This result holds if the elastic constants are the same for the matrix and the inclusion. The full deformation tensor is $\alpha_{ij} = \frac{\partial u_i}{\partial r_j}$, and the strain tensor ϵ_{ij} is the symmetric part of α_{ij}. The resulting shear strain outside of the inclusion core, expressed in cylindrical coordinates, is:

$$\epsilon_{yz}(r,\theta,x) = \frac{a^3\epsilon^0_{yz}}{4(r^2+x^2)^{9/2}}(9a^2cr^4 - (2+3c)r^6 + 9cr^2(-8a^2+5r^2)x^2 + \\ 6(r^2+4c(a^2+r^2))x^4 + 4(1-6c)x^6 + 15cr^4(-7a^2+5(r^2+x^2))\cos(4\theta)) \tag{A.5}$$

where as above $\mathbf{r}(y,z)$ is the position vector from the center of the inclusion and $\theta = \cos^{-1}(z/r)$.

ACKNOWLEDGMENTS

This work was supported by National Science Foundation through the Harvard MRSEC (Contract #DMR-0820484) and by Contract #DMR-1206765. We thank John Hutchinson for help with the mechanics of the Eshelby inclusion, Roderick W. Jensen for assistance in preparing Figures 6 and 7, and Peter Schall for many useful discussions.

---

[1] F. Spaepen, Acta Metall. **25**, 407 (1977).

[2] A. S. Argon, Acta Metall. **27**, 47 (1979).

[3] G. Picard, A. Ajdari, F. Lequeux, and L. Bocquet, Eur. Phys. J. E **15**, 371 (2004).

[4] J. S. Langer, Phys. Rev. E **85**, 051507 (2012).

[5] M. L. Falk and J. S. Langer, Phys. Rev. E **57**, 7192 (1998).

[6] C. E. Maloney and A. Lemaître, Phys. Rev. E **74**, 016118 (2006).

[7] A. Tanguy, F. Leonforte, and J.-L. Barrat, Eur. Phys. J. E **20**, 355 (2006).

[8] A. Lemaître and C. Caroli, Phys. Rev. Lett. **103**, 065501 (2009).

[9] J. Chattoraj and A. Lemaître, Phys. Rev. Lett. **111**, 066001 (2013).

[10] A. L. Greer and E. Ma, Mater. Res. Bull. **32**, 611 (2007).

[11] P. S. Schall, D. A. Weitz, and F. Spaepen, Science **318**, 1895 (2007).

[12] V. Prasad, D. Semwogerere, and E. R. Weeks, J. Phys.: Cond. Matt. **19**, 113102 (2007).

[13] K. E. Jensen, D. Pennachio, D. Recht, D. A. Weitz, and F. Spaepen, Soft Matter **9**, 320 (2013).

[14] P. Schall, I. Cohen, D. A. Weitz, and F. Spaepen, Science **305**, 1944 (2004).

[15] P. Schall, I. Cohen, D.A. Weitz, and F. Spaepen, Nature **440**, 319 (2006).

[16] P. Schall and F. Spaepen, in *Dislocations in Solids*, edited by J.P. Hirth and L. Kubin (Elsevier, New York, 2010), p. 233.

[17] P. Schall and F. Spaepen, Int. J. Mater. Res. **97**, 958 (2006).

[18] M. C. M. Persson Gulda, Ph.D. Thesis, Harvard University, 2013.

[19] V. Chikkadi, G. Wegdam, D. Bonn, B. Nienhuis, and P. Schall, Phys. Rev. Lett. **107**, 198303 (2011).

[20] J. D. Eshelby, Proc. R. Soc. A **241**, 376 (1957).

[21] J. D. Eshelby, Proc. R. Soc. A **252**, 561 (1959).

[22] We purchase specially-filtered Sicaster plain particles from Micromod (www.micromod.de) According to the manufacturer, the particles have an average diameter $2\bar{R} = 1.55$ μm. The polydispersity is measured by fitting the first peak of the radial distribution function from a densely-packed sample and deconvolving to obtain the particle size distribution.

[23] J. D. Bernal, I. A. Cherry, J. L. Finney, and K. R. Knight, J. Phys. E **3**, 388 (1970).

[24] K. E. Jensen, Ph.D. Thesis, Harvard University, 2013. The amorphous templates are described on pg. 49-53; the iterative particle locating algorithm is described on pg. 25-27.

[25] N. Nakamura, K. E. Jensen, D. A. Weitz, and F. Spaepen (in preparation).

[26] Note that we use the conventional mechanical testing definition of yield, which refers to the onset of irreversible deformation. This differs from the rheological definition of yield, which instead refers to the strain at which the viscous response of the material begins to dominate over the elastic, that is, when the loss modulus G'' exceeds the storage modulus G'.

[27] W.L. Johnson and K. Samwer, Phys. Rev. Lett. **95**, 195501 (2005).

[28] G. Petekidis, A. Moussaïd, and P.N. Pusey, Phys. Rev. E **66**, 051402 (2002).

[29] L. Mohan, C. Pellet, M. Cloitre, and R. Bonnecaze, J. Rheol. **57**, 1023 (2013).

[30] E.D. Knowlton, D.J. Pine, L. Cipelletti, arXiv:1403.4433v1.

[31] D. Fiocco, G. Foffi, and S. Sastry, Phys. Rev. E **88**, 020301(R) (2013).

[32] C.F. Schreck, R.S. Hoy, M.D. Shattuck, and C.S. O'Hern, Phys. Rev. E **88**, 052205 (2013).

[33] N. Perchikov and E. Bouchbinder, Phys. Rev. E **89**, 062307 (2014).

[34] Y. Gao and M.L. Kilfoil, Opt. Express **17**, 4685 (2009). We use the locating software described in this publication, which is available under "MATLAB 3D feature finding algorithms" at http://people.umass.edu/kilfoil/downloads.html.

[35] K. E. Jensen, D. A. Weitz, and F. Spaepen, Rev. Sci. Instrum. **84**, 016108 (2013).